



# Anisotropic molecular scattering at microstructured surface for rarefied gas compression inside air breathing ion engine

Kosuke Shoda<sup>1</sup> · Naoki Kano<sup>1</sup> · Yuki Jotaki<sup>1</sup> · Keisuke Ezaki<sup>1</sup> · Kazuki Itatani<sup>1</sup> · Takashi Ozawa<sup>2</sup> · Yusuke Yamashita<sup>3</sup> · Kazutaka Nishiyama<sup>4</sup> · Kumiko Yokota<sup>1</sup> · Masahito Tagawa<sup>1</sup>

Received: 8 July 2021 / Revised: 1 February 2022 / Accepted: 1 February 2022 / Published online: 1 March 2022  
© CEAS 2022

## Abstract

The effect of the micro-structure surface on the passive compression performance of the intake system of an air-breathing ion engine (ABIE) system is proposed and analysed. The scattering distributions of the thermal Ar beam pulses at the microstructure surface were measured experimentally. The scattering process at the microstructure surface demonstrated anisotropic nature at a grazing angle of incidence; however, it demonstrated a complex scattering pattern due to the multiple bounce effect at the facet surface, despite each scattering pattern being similar to that on the flat surface. The DSMC calculation at an altitude of 250 km was also performed using the simple scattering model, which is based on the experimental results of scattering distribution and recent ABIE design. The computational results indicate that the compression performance of the microstructure intake is higher than that of the diffusive and specular flat intakes.

**Keywords** Very low earth orbit · VLEO · Air breathing ion engine · ABIE · Molecular scattering · Microstructure

## 1 Introduction

The use of low-altitude satellites has expanded rapidly in recent years for Earth observation, navigation, and communications. It has been recognized that high-resolution observations and low-energy communications are realized by orbiting lower altitudes called very low Earth orbit (VLEO) or sub-LEO. However, the increased atmospheric drag due to the dense atmosphere limits long-term satellite operations in sub-LEO in the absence of propulsion systems. Recent attempts to operate satellites in sub-LEO, such as the Gravity Field, Steady-State Ocean Circulation Explorer (GOCE) [1], and Super Low Altitude Test Satellite (SLATS) [2], used electric thrusters to compensate for atmospheric drag. The

mission lives of these satellites are limited by the amount of propellant on board. In general, a longer operation of a satellite in sub-LEO requires a large propellant tank, increasing the satellite size and atmospheric drag. A large atmospheric drag force requires a large thruster system to compensate, thereby consuming more propellant and electric power. Such a large thruster system produces a large atmospheric drag.

To resolve the aforementioned issues, the concept of “propellant collecting thrusters” has been considered since 1960s by many researchers [3, 4]. However, the idea was never realized. A historical survey is provided in the literature [5]. However, significant progress in the propellant collecting thruster concept was made by Nishiyama in 2003 [6]. The air breathing ion engine (ABIE) integrates a high-efficiency passive compression intake system and an electron cyclotron resonance (ECR) ion engine. This ECR ion engine system was applied to Hayabusa and Hayabusa2 planetary probes, and exhibited high performance and reliability [7]. Therefore, an unsolved problem that persists is the design of a high-efficiency passive compression intake system. A high-efficiency passive compression intake system is a key technology for all propellant-collecting thruster systems, in addition to ABIE. Recently reported air breathing electric propulsion (ABEP) also requires a high-efficiency intake system [8]. A high-efficiency intake system is required to

✉ Masahito Tagawa  
tagawa@mech.kobe-u.ac.jp

<sup>1</sup> Graduate School of Engineering, Kobe University,  
Kobe 657-8501, Japan

<sup>2</sup> Japan Aerospace Exploration Agency, Chofu 182-8522,  
Japan

<sup>3</sup> Department of Aeronautics and Astronautics, The University  
of Tokyo, Sagamihara 252-5210, Japan

<sup>4</sup> Institute of Space and Astronautical Science, Japan  
Aerospace Exploration Agency, Sagamihara 252-5210, Japan

achieve high transmittance of incoming molecules and low transmittance of outgoing molecules to produce maximum thrust. It also needs to equip high-compression performance to operate at high altitudes, where the molecular density is insufficient to maintain the plasma. Therefore, the former performance is more important for large systems operated at relatively lower altitudes (high atmospheric density environments), and the latter performance is added for small systems operating at higher altitudes (low atmospheric density environments). ABIE targets a higher altitude to operate, so that high-compression performance is achieved.

It has been recognized that ground-based experiments are quite important for ABIE development; however, there are challenges in reproducing atmospheric conditions in sub-LEO using ground-based facilities, such as velocity, composition, density, and charged impurities in the beam, in the ground evaluation of the intake system. Even in such a difficult situation, the development of a high-efficiency passive compression intake system is still in progress. As for the ground-based experiment of ABIE, ECR plasma ignition with hyperthermal  $N_2$  and AO beam pulses at 8 km/s was first demonstrated in 2009 [9] and published later [10]. In this experiment, a laser-detonation beam source, which has been widely used in the field of material erosion studies in LEO, was applied [11–13]. An original high-efficiency passive compression intake was experimentally tested by Tagawa and Nishiyama [10]. They used a straw-like collimator, which allows flow-in hyperthermal directional molecules from outside the inlet and prevents the flow-out of randomly moving molecules with thermal velocity through the collimator. The effect of the collimator to prevent back-streaming molecules was experimentally verified [10]. An

important aspect of the intake design is to achieve the maximum conductance of the incoming flow and the minimum conductance of the outgoing flow in the intake; however, the scattering event at the collimator surface itself is isotropic in the moving directions of the molecules. Many molecular scattering experiments were performed in the field of surface science in the past; however, they targeted clean ideal flat surfaces to realize the surface physics and chemistry [14, 15]. Our idea is that macroscopically anisotropic scattering behaviour might be realized at the surface covered by microscopic facets. However, fundamental relationships between scattering distribution and surface morphology to achieve the anisotropic nature of surface scattering has not been established or explored.

In this study, we propose the use of microstructures on the intake surface of ABIE to achieve anisotropic scattering properties. A scattering experiment on the microstructure surface was performed to demonstrate this effect, and DSMC calculations were applied to evaluate the advantages of the compression performance of the microstructure intake system, based on the results of molecular scattering experiments.

## 2 Molecular scattering experiments

A schematic illustration of the experimental apparatus is shown in Fig. 1. This facility was used in the first ignition experiment for ABIE in 2009 [9]. The experimental facility consists of three vacuum chambers, referred to as the source, reaction, and time-of-flight (TOF) chambers from upstream. Molecular beam pulses are formed by a house-made pulsed

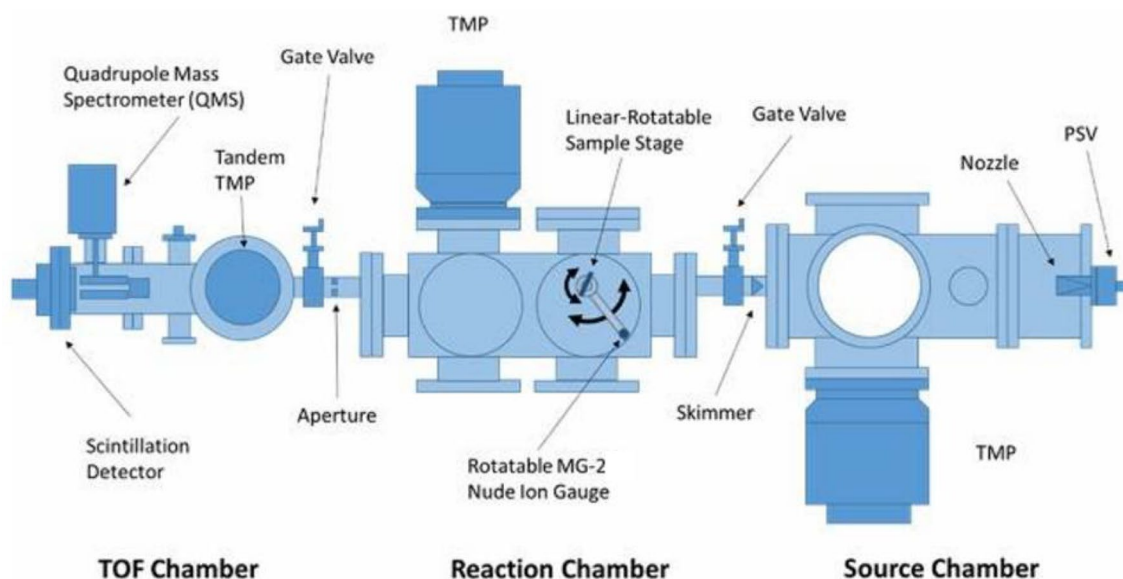


**Fig. 1** Schematic drawing of the experimental facility used in the rarefied gas scattering experiment

supersonic valve (PSV) attached to the source chamber [16, 17]. The PSV is capable of ejecting a gas pulse with a typical thermal velocity of 3 Hz. A laser-detonation system can form hyperthermal beam pulses at the orbital velocity of the spacecraft (8 km/s); however, all the experiments reported in this study were performed using thermal velocity because most of the molecules in the intake were in thermal equilibrium conditions. No  $\text{CO}_2$  laser was used in this experiment. An atomic oxygen beam pulse, which is the major component of the sub-LEO region, cannot be applied in thermal beam experiments because the laser energy for acceleration is also necessary for dissociating  $\text{O}_2$  molecules into AO. Thus, Ar was used as the gas pulse in this experiment. An Ar pulse was introduced to the source chamber through a conical nozzle, and then to the reaction chamber through a 3 mm skimmer. The scattering distribution measuring

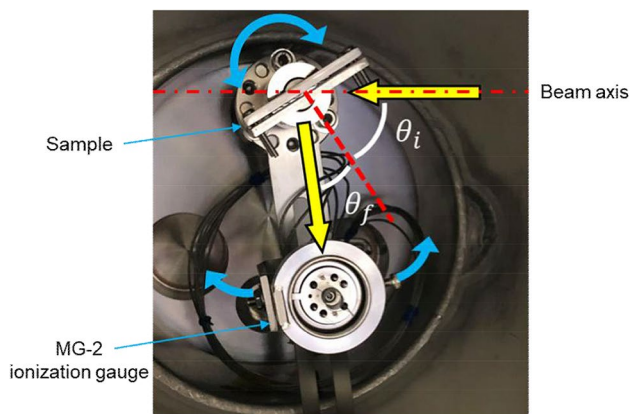
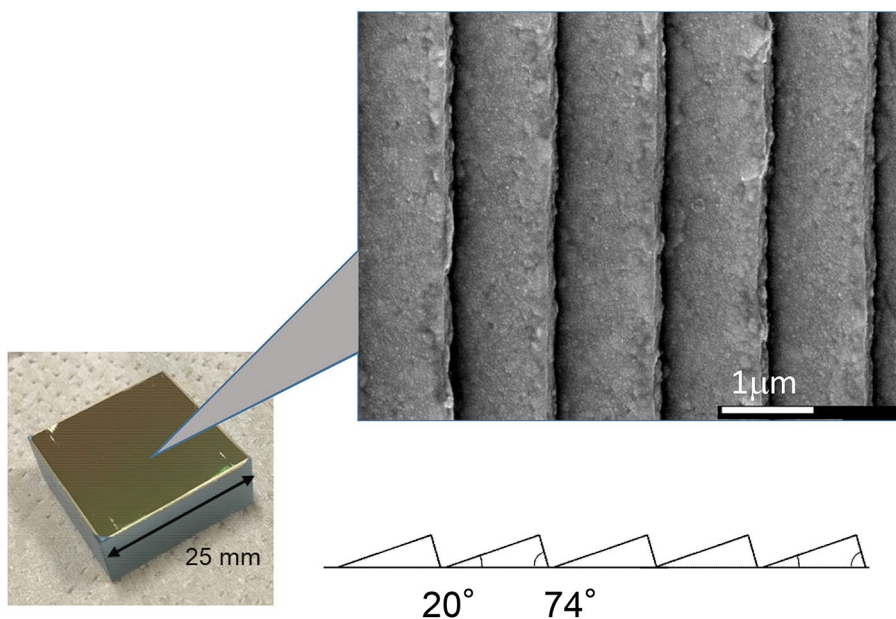


**Fig. 2** MG-2 ionization gauge and sample mounted on the coaxial  $z\theta$  stage. Incident and final angles and defined as shown in the figure

**Fig. 3** Photograph and SEM image of the microstructured surface. The facet angles are  $20^\circ$  and  $74^\circ$  and the periodic length is  $1.2\ \mu\text{m}$



system was designed and attached to the reaction chamber (Fig. 2). To install the entire measurement system in the reaction chamber, the system was designed to be simple, compact, and mounted on a single ICF-203 flange. This system consisted of a retractable/rotatable sample holder and a rotatable ionization gauge. A retractable mechanism is required when the TOF system in the TOF chamber is used for the laser detonation AO beam experiment. The sample was mounted on the inner rod of the coaxial  $\theta z$  stage (linear and rotation feedthrough), and the modified MG-2 (Canon Anelva Corp., Japan) ionization gauge was mounted on the detector arm attached to the outer rotatable cylinder located in the reaction chamber. The distance between the sample surface and the ionization gauge (flight length) was 70 mm, while the distance between the nozzle and sample surface was 1250 mm. The ionization area of MG-2 (grid diameter) was 6 mm, and the detection angle resolution of this system was expected to be  $5^\circ$ . The angular resolution is not very high because of the short flight length of 70 mm; however, it enables the detection of the ion current by a simple analogue circuit. The filament and grid of the modified MG-2 ionization gauge was controlled by the original electronics of the MG-2 ionization gauge; however, the ion current from the ion collector was directly measured by a digital storage oscilloscope after amplification by a fast current–voltage preamplifier SA-606F2 (NF Corp., Japan). The base pressure of the reaction chamber was lower than that of  $3\text{E-}7$  Pa.

Figure 3 shows an SEM photograph of the microstructure surface tested in this experiment. To demonstrate the effect of the microstructure at the surface on the scattering pattern, we chose a brazed grating as the sample surface (Edmond Optics, USA). A one directional groove with a triangular cross-section is formed on the sample surface with

**Table 1** Samples used in this study

	Au-coated mirror	Microstructured surface
Surface coating	Au	Au
Substrate material	Cu	Float glass
Facet angle (°)	–	20
Facet angle (°)	–	74
Periodic length (μm)	–	1.2
Size and shape	25 mm in dia	25 × 25 mm in square

**Table 2** Conditions of scattering experiments

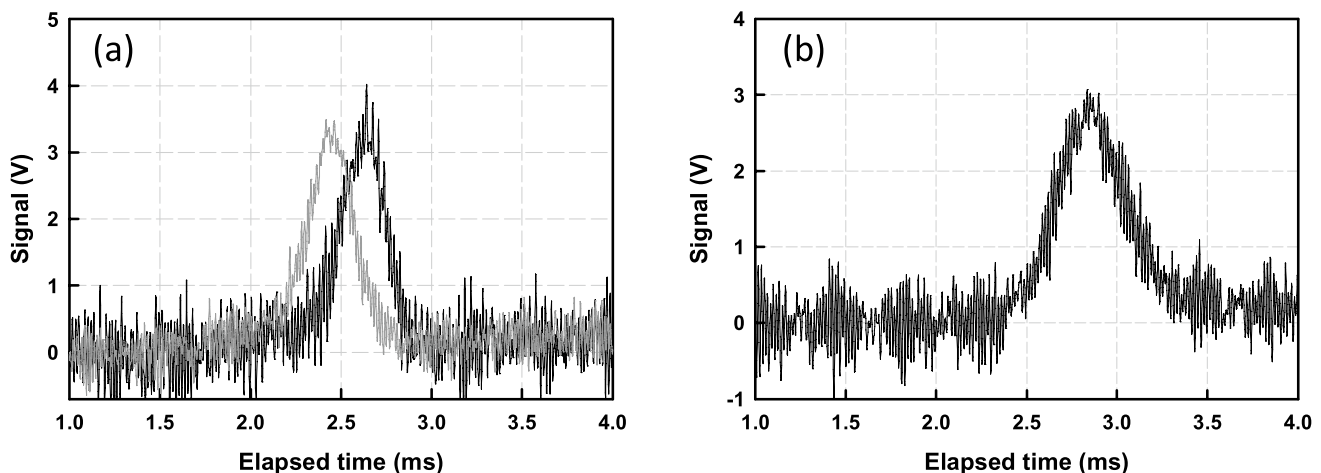
Incident species	Ar
PSV pressure (Pa)	35
Distance between PSV and sample (mm)	1250
Distance between sample and ionization gauge (mm)	70
Base pressure (Pa)	3E-7
Repetition rate (Hz)	3
Sample temperature	Room temp

a periodic length of 1.2 μm. A cross-sectional view of the sample surface structure is shown in Fig. 3. The surface was covered by a facet structure at 20° and 74°. The top surface was coated with an Au layer. To analyse the effect of the microstructure on the scattering distribution, a flat Au mirror from the same manufacturer was used for comparison purposes. The details of the sample are listed in Table 1. The temperature of the sample surface was not controlled; however, it was confirmed that the temperature of the samples did not change during the Ar beam exposure. The experimental conditions are presented in Table 2. In the following section, the incident angle ( $\theta_i$ ) and final angle ( $\theta_f$ ) are defined as those relative to the surface normal direction (see Fig. 2).

### 3 Experimental results

Figure 4a shows the TOF spectra of the incident Ar beam measured by the modified MG-2 detector at 1180 and 1320 mm downstream from the nozzle (the TOF system shown in Fig. 1 was not used). Note that the TOF at 1320 mm was measured by retracting the sample holder from the beam line. The measurement signal was accumulated for 400 pulses, and clear signals of the incident beam were detected. Time zero is when the PSV is triggered to open. The velocity of the incident beam was calculated from the time difference between these two peaks (0.30 ms) at two positions (140 mm). The result was 470 m/s, which is higher than the expected thermal velocity of Ar at 300 K (353 m/s), probably due to the PSV settings, such as the back pressure and/or opening voltage. When the sample was inserted in the beam line at 1250 mm, the incoming beam hit the surface at 2.52 ms. This is flight time = 0 for the scattered atom. Figure 4b shows the TOF spectrum of the Ar beam scattered at the Au flat mirror surface at 1250 mm, with an incident angle  $\theta_i = 60^\circ$  and a final angle  $\theta_f = 60^\circ$ . As indicated, the peak was broadened by the scattering (FWHM changes from 0.29 to 0.41 ms) and peak position (2.82 ms), which reveals a flight time of 0.30 ms for 70 mm after the scattering event. The velocity of the scattered Ar atom was determined to be 230 m/s; however, it was too slow as a thermal equilibrium velocity ejected from the Au surface at room temperature. The cause of this analytical result is not specified at this point; however, it might be implied that Ar atoms experience complicated scattering processes, including multiple bounce effects and/or large surface accommodation times during the scattering event.

To evaluate the Ar flux of the scattered atom accurately, it is necessary to compensate the ionization probability

**Fig. 4** Typical TOF spectrum recorded on the digital storage scope



with velocity, which is proportional to the sojourn time of molecules in the ionization of the MG-2 detector (flux weighted-TOF spectra). However, insufficient time-resolution of the TOF spectrum, accompanied by the operation of PSV, which creates an incident beam with a FWHM of 0.29 ms, provides errors in the flux weighted-TOF spectra. The diameter of the MG-2 detector (6 mm), which is 9% of the flight length, also caused a large FWHM of the measured spectra. Therefore, we consider the area of the TOF spectra, which is not compensated by the ionization probability with velocity, as being equivalent to the flux of scattered Ar. This assumption would provide additional error in flux distribution; however, it is still possible to achieve a qualitative analysis of the scattering pattern.

Figure 5 shows the polar plot of the distributions of the thermal Ar beam scattered at the Au-coated flat surface. The radial axis indicates the relative area of the TOF spectra measured at each final angle. The measurement was performed at incident angles  $\theta_i$  at  $0^\circ$ ,  $30^\circ$ , and  $60^\circ$ , as indicated by the blue arrow in the plot. Solid circles show the raw data, and the grey circle is the best-fit diffusive component. The white squares are the residual component representing the non-diffusive scattering (result of subtraction of diffusive component from raw data in each final angle). It was observed that the scattering distribution of the  $0^\circ$  incidence

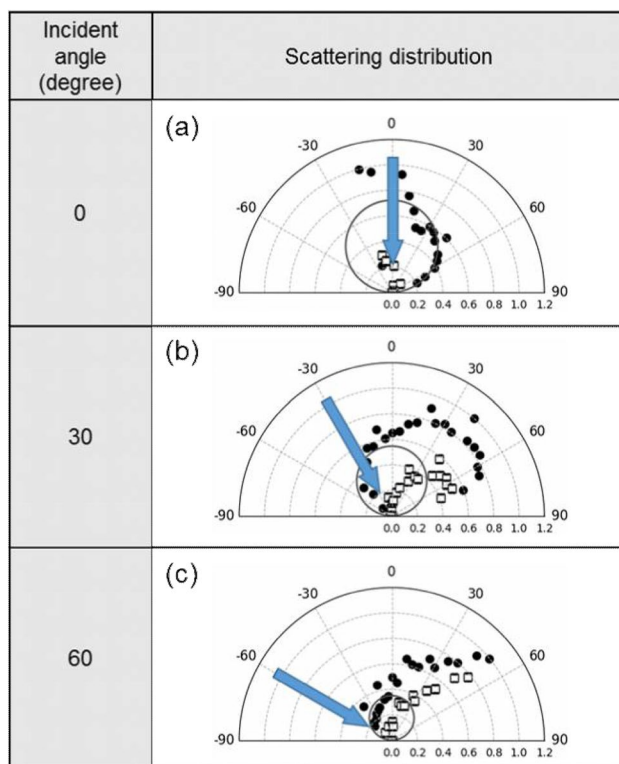
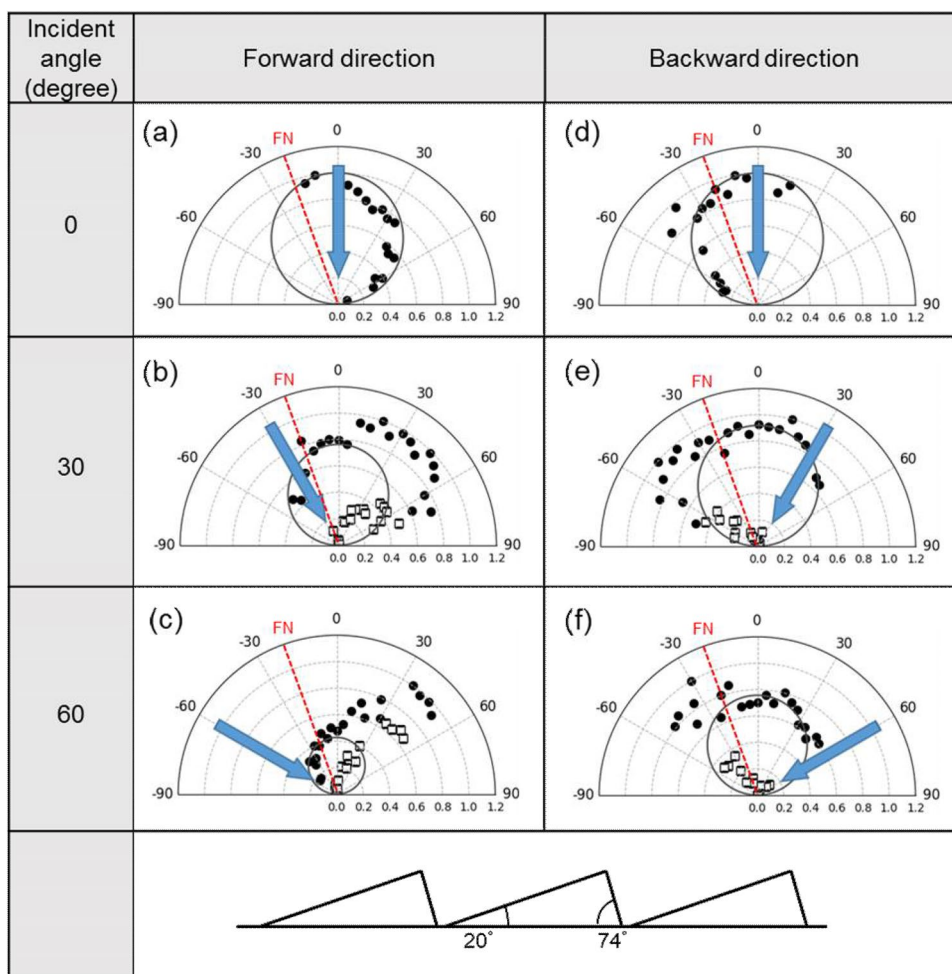


**Fig. 5** Scattering distributions of thermal Ar beam scattered on the Au-coated flat surface at room temperature. Solid circle, raw data; grey circle, diffusive component and square, non-diffusive component

(Fig. 5a) follows diffusive scattering, and only small non-diffusive component is observed at the final angle near  $0^\circ$  (specular direction). The accommodation coefficient (fraction of diffusive component in the whole scattering molecules) was calculated to be 0.95, which is almost fully diffusive scattering. However, the non-diffusive component increases in the specular direction as the incident angle increases, especially at larger final angles, as shown in Fig. 5b and c. The accommodation coefficient decreases to 0.63 and 0.58 for Fig. 5b and c, respectively. It should be mentioned that the accommodation coefficients of Fig. 5b and c are evaluated to be larger than the real values because scattering data at large final angles ( $+60^\circ$  to  $+90^\circ$ ) which involve large fraction of non-diffusive component is not included in the calculation. From the scattering distribution observed in Fig. 5, it was observed that the Ar atoms scattered at the Au surface used in this experiment show scattering patterns that are a mix of diffusive and non-diffusive components, depending on the incident angle. More non-diffusive component (lobular-like patterns) is included at large incident angles.

Figure 6 shows the distributions of the thermal Ar beam scattered at the Au-coated microstructure surface, as shown in Fig. 3. The measurement was performed at macroscopic incident angles of  $0^\circ$ ,  $30^\circ$ , and  $60^\circ$ , against the substrate (not a facet surface). The blue arrows in the figures show the directions of the incident beams, and FN represents the direction of the facet normal. The shape of the microstructure is shown at the bottom of the figure. Solid circles show the raw data, and the grey circle is the best-fit diffusive component. The white square is the residual component representing the non-diffusive scattering. At macroscopically normal incidence, the scattering patterns are similar to diffused scattering (Fig. 6a and d). However, no lobular component was observed, as shown in Fig. 5a. A small specular component is observed at  $-40^\circ$  in Fig. 6d while considering the fact normal directions at  $-20^\circ$ , even though it is not very clear. It was concluded from Fig. 6a and d that the scattering distribution at the microstructure surface is similar to that of the flat surface at an incident angle of  $0^\circ$ . Similar scattering patterns to the flat surface were also observed at incident angles of  $-30^\circ$  and  $-60^\circ$  (forward direction, Fig. 6b and c). The direction of non-diffusive scattering became shallow owing to the angle of the facet, as shown in Figs. 6b and c. The accommodation coefficients of these two cases were calculated to be 0.75 and 0.64, which are almost identical to those at the flat Au surface. In contrast, the scattering distributions of the backward directions (Figs. 6e and f) indicate a more diffusive component compared to those of forward scattering cases (accommodation coefficient of 0.87 for both cases). We expected a non-diffusive scattering peak in the  $+60^\circ$  direction in Fig. 6f because it is grazing angle incidence to the facet surface; however, this was not observed. This was probably due to the close to the normal incidence to the wall of the facet, which leads to diffusive scattering to the

**Fig. 6** Scattering distributions of thermal Ar beam scattered at the Au-coated microstructured surface at room temperature. Blue arrows show the directions of the incident beam and FN represent the direction of the facet normal. The direction of the microstructure is indicated at the bottom of the figures. Solid circle, raw data; grey circle, diffusive component and square, non-diffusive component

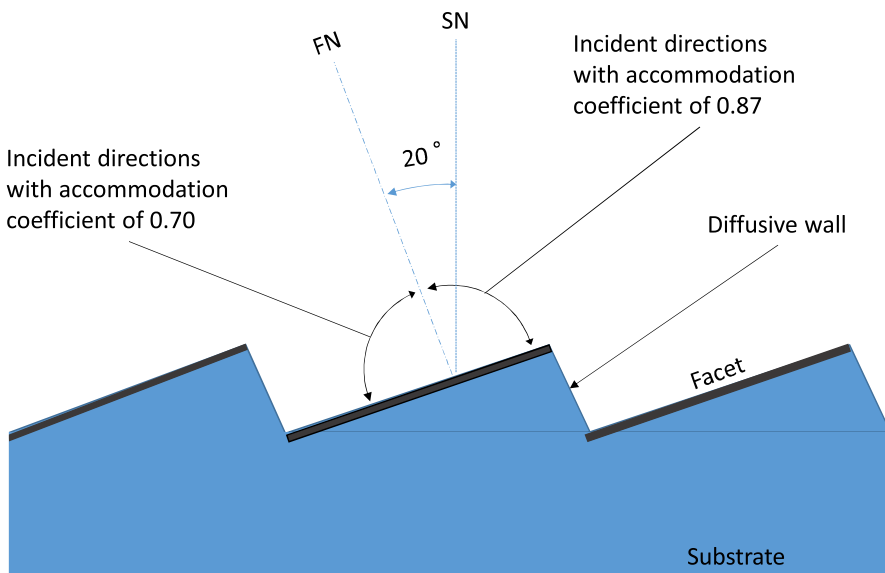


wide final angles and/or multi-bounce effect at the neighbouring facet surfaces. The rapid decrease at  $-60^\circ$  in Fig. 6e and f is also due to the shadowing effect of the neighbouring facet. The shadowing effect of the neighbouring facet prevented the non-diffusive scattering of Ar atoms from colliding in backward directions, creating anisotropic scattering properties at the microstructured surface. From a series of scattering experiments, Ar scattering at the microstructure surface is concluded as follows: (1) In the forward direction, the scattering properties are similar to those on flat surfaces, that is, diffusive at small incident angles and the non-diffusive component becomes large at large incident angles; (2) in the backward directions, scattering properties were more diffusive than in the forward direction, and Ar atoms with large final angles were blocked by the shadowing effect.

#### 4 DSMC simulation for compression performance on ABIE

From the series of scattering experiments shown in the previous section, the complex scattering properties at the microstructured surface were observed. To evaluate this unique scattering property of the microstructure surface on the compression performance of the intake system for ABIE, the direct simulation Monte Carlo (DSMC) method was applied. According to the results of the scattering experiment, a scattering model based on the Maxwell model was used in the DSMC calculation: incident molecules with macroscopic incident angles between  $+90^\circ$  and  $-20^\circ$  follow the diffusive scattering

**Fig. 7** Reflection model used in the DSMC calculation. SN and FN indicate the macroscopic surface normal and microscopic facet normal



with an accommodation coefficient of 0.87; however, incident angles between  $-20^\circ$  (FN direction) and  $-90^\circ$  exhibit specular scattering with an accommodation coefficient of 0.70, as shown in Fig. 7. The other facet surfaces are configured as 100% diffusive surfaces, owing to the low possibility of large incident angle scattering and small areas.

The computational code of the DSMC used in this study was developed in the laboratory, and was successfully used in ECR ion engine development at The University of Tokyo [18]. The double cylindrical ABIE model proposed by Ozawa (Fig. 8) [19] was used as the ABIE model. This

model was designed based on the use of  $\mu 10$  ECR ion engines developed at ISAS/JAXA. The basic concept is that the molecules are collected from the intake on the left side of the figure and compressed in the long intake system composed of the inner and outer cylinders. Molecules passing through the intake system were introduced into the accommodation and discharge chambers. The long channel of intake prevents the backflow of molecules by diffusive scattering at the surface.

The conditions used in the DSMC calculations are listed in Table 3. The operation of the ABIE at an altitude of 250 km is assumed. Atmospheric conditions were

**Fig. 8** Cross-section of the double cylindrical ABIE used for DSMC calculation [15]

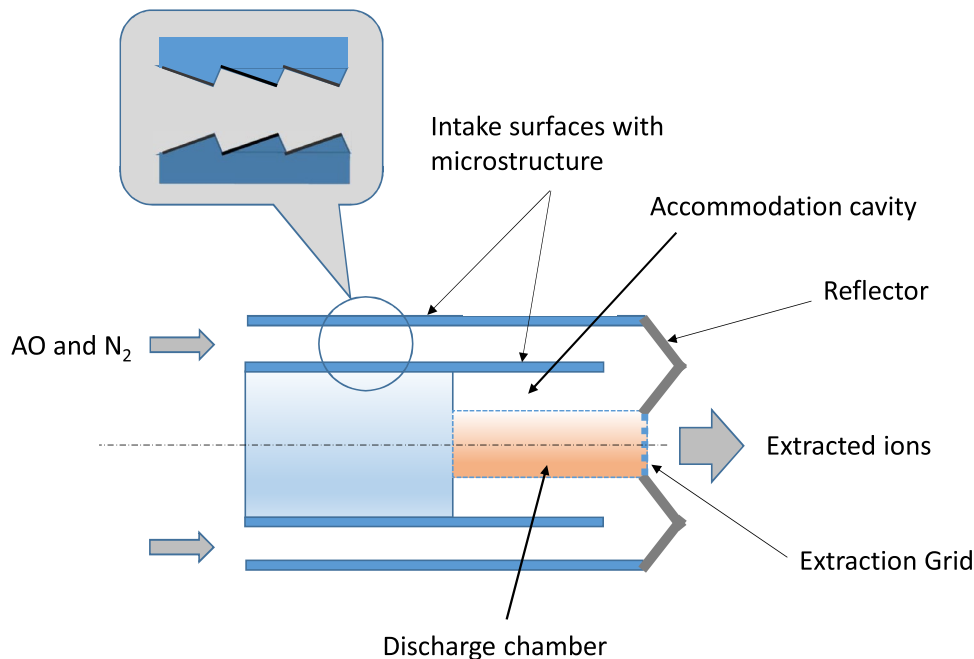


**Table 3** Simulation conditions for compression performance evaluation

ABIE model	Double cylindrical type
Altitude (km)	250
Number density ( $\text{m}^{-3}$ )	$1.43 \times 10^{15}$
Inflow velocity (m/s)	7754
Atmospheric temperature (K)	839.6
Wall temperature (K)	300.0
Gas-surface interaction model (except intake surface)	Diffuse
Mass of molecule (kg)	$3.26 \times 10^{-26}$
Transmittance (entrance of discharge chamber)	0.5
Transmittance (extraction grid)	0.2

**Table 4** Compression performance calculated by DSMC

Intake surface	Microstructured surface	Flat surface	
		Diffusive	Specular
Compression ratio	175	146	45

obtained from NRLMSISE-00 predictions. The diffuse reflection scheme was applied to all surfaces besides intake. The transmittances from the accommodation cavity to the discharge chamber and the extraction grid system are assumed to be 0.5 and 0.2, respectively [19]. The ABIE model (290 mm diameter in diameter and 610 mm in length) was located at the centre of the cylindrical computational area (800 mm in diameter and 800 mm in length). No interaction between molecules was considered due to their low molecular density. The trajectory of the  $1.1\text{E}+6$  atoms was chased in every  $1\text{E}-7$  s for  $1\text{E}+6$  steps.

The compression performance was evaluated by the compression ratio  $G$ , which is defined by the ratio of number densities in the discharge chamber ( $n_{\text{dis}}$ ) and those outside the ABIE ( $n_{\text{atm}}$ ).

$$G = \frac{n_{\text{dis}}}{n_{\text{atm}}} \quad (1)$$

Calculations were performed in three cases: (1) inside the intake surfaces covered by the microstructured surface and (2) covered by a normal flat surface with 100% diffuse or (3) with 100% specular scattering scheme. Table 4 presents the calculation results. The flat intake surfaces at 100% diffusive and 100% specular scattering properties provide compression ratios of 146 and 45, respectively. The low compression ratio at 100% specular intake indicated that the specular surface did not prevent the backflow of the molecules. By applying the microstructure surface to the intake surface, the compression ratio increased to 175, which was 20% greater than the 100% diffusive surface, and 3.9 times greater than the specular surface. It is thus concluded that the application of a microstructured surface is advantageous for achieving

high compression performance in ABIE, even though the result is obtained with rough DSMC modelling, and non-optimized shape and material of the microstructure. The optimisation of the shape, such as facet angle, surface material, and DSMC modelling, will provide better and more accurate results on the compression performance of ABIE intake.

## 5 Conclusions

The effect of the microstructure surface on the passive compression performance of the intake system of an air-collecting thruster system was proposed and evaluated. The scattering distribution of the thermal Ar beam pulse was measured experimentally using a compact scattering measurement system attached to a laser-detonation atomic oxygen beam system. It was confirmed that the scattering distribution is basically a combination of diffuse and lobular patterns; however, the scattering process at the microstructure surface is complex because of the multiple bounce effect at the facet surface, even though each scattering is similar to that at a flat surface. The DSMC calculation at an altitude of 250 km was performed using the simple scattering model, which was based on the experimental results and recent ABIE design. It was observed that the compression performance of the intake increased at the microstructure surface, as compared to the diffusive surface, by 20%, which is important for ABIE application in its operation at altitudes of 250 km, which is a relatively high altitude as a propellant-collecting thruster system. The optimisation of the shape and material of the microstructure was not performed in this study; however, it was demonstrated in this study that the application of the microstructure surface has the potential to obtain high compression performance of ABIE intake.

**Acknowledgements** The authors would like to thank Professor T. K. Minton (University of Colorado, Boulder) for their valuable discussions. Part of this work was supported by KAKENHI from JSPS under contracts #18K18912, #18H01624, #19K22017, and 19H02346.



**Funding** Japan Society for the Promotion of Science.

**Availability of data and materials** N/A.

**Code availability** N/A.

## Declarations

**Conflicts of interest** The author(s) declare that they have no conflict of interests.

## References

1. GOCE home page: [http://www.esa.int/Our\\_Activities/Observing\\_the\\_Earth/GOCE](http://www.esa.int/Our_Activities/Observing_the_Earth/GOCE) (2020)
2. Imamura, S., Utashima, M., Ozawa, T., Akiyama, K., Sasaki, M.: Current status of the on-going orbit transfer of super low altitude test satellite (SLATS). In: Proceedings of the 69th International Astronautical Congress, IAC-18-C1.8.1. Bremen, Germany (2018)
3. Cara D., Amo G., Santovincenzo A., Dominguez B., Arcioni M., Roma A.: RAM electric propulsion for low earth orbit operation. In: an ESA Study, IEPC-2007-162 (2007)
4. Cifali G., Misuri T., Rossetti P., Andrenucci M., Valentian D., Feili D., Lotz B.: Experimental characterization of HET and RIT with atmospheric propellants. In: Proceedings of 32nd International Electric Propulsion Conference, Wiesbaden, Germany, IEPC-2011-224 (2011)
5. Zheng, P., Wu, J., Zhang, Y., Wu, B.: A comprehensive review of atmosphere-breathing electric propulsion systems. *Int. J. Aerosp. Eng.* **2020**, 1–21 (2020)
6. Nishiyama K.: Air breathing ion engine concept. In: Proceedings of the 54th international astronautical congress of the international astronautical federation, the International Academy of Astronautics, and the International Institute of Space Law, Bremen, Germany, IAC-03-S.4.02 (2003). doi: 10.2514/6. IAC-03-S.4.02
7. Coral, G., Tsukizaki, R., Nishiyama, K., Kuninaka, H.: Microwave power absorption to high energy electrons in the ECR ion thruster. *Plasma Sourc. Sci. Technol.* **27**, 095015 (2018)
8. Romano, F., Espinosa-Orozco, J., Pfeiffer, M., Herdrich, G., Crisp, N.H., Roberts, P.C.E., Holmes, B.E.A., Edmondson, S., Haigh, S., Livadiotti, S., Macario-Rojas, A., Okio, V.T.A., Sinpetru, L.A., Smith, K., Becedas, J., Sulliotti-Linner, V., Bisgaard, M., Christensen, S., Hanessian, V., Kaufman-Jensen, T., Nelson, J., Chan, Y.A., Fasoulas, S., Traub, C., Garcia-Alminana, D., Rodrigues-Donaire, S., Sureda, M., Kataria, D., Belkouchi, B., Conte, A., Seminari, S., Villain, R.: Intake design for an atmosphere-breathing propulsion system (ABEP). *Acta Astronaut.* **187**, 225–235 (2021)
9. Tagawa M., Nishiyama K., Yokota K., Yoshizawa Y., Yamamoto D., Kuninaka H.: An experimental study on air breathing ion engine using a laser-detonation atomic oxygen beam source as LEO space environment simulator. In: The 27th International Symposium on Space Technology and Science, Tsukuba, Japan, 2009.07.05–07.12, on USB Memory (2009)
10. Tagawa, M., Nishiyama, K., Yokota, K., Yoshizawa, Y., Yamamoto, D., Tsuboi, T., Kuninaka, H.: Experimental study on air breathing ion engine using laser detonation beam source. *J. Propul. Power* **29**, 501–506 (2013)
11. Yokota, K., Tagawa, M., Fujimoto, Y., Ide, W., Kimoto, Y., Tsuchiya, Y., Goto, A., Yukumatsu, K., Miyazaki, E., Imamura, S.: Effect of simultaneous N<sub>2</sub> collisions on atomic oxygen-induced polyimide erosion in sub-low Earth orbit: comparison of laboratory and SLATS data. *CEAS Space J* **13**, 389–397 (2021). <https://doi.org/10.1007/s12567-021-00358-4>
12. Tagawa, M., Yokota, K., Kishida, K., Okamoto, A., Ishizawa, J., Minton, T.K.: Effect of ultraviolet emission from the oxygen plasma on the accelerated erosion phenomenon of fluorinated polymer in the atomic oxygen ground tests. *High Perform. Polym.* **22**, 213–224 (2010)
13. Kenoshita, H., Tagawa, M., Yokota, K., Ohnae, N.: Nonlinear phenomenon in the mass-loss of polyimide film under hyperthermal atomic oxygen beam exposure. *High Perform. Polym.* **13**, 225–234 (2001)
14. Muino, R.D., Busnengo, H.F. (eds.): Dynamics of Gas-Surface Interactions. Springer, Berlin (2013)
15. Mehta, N.A., Murray, V.J., Xu, C., Levin, D.A., Minton, T.K.: *J. Phys. Chem. C* **122**, 9859–9874 (2018)
16. Tagawa, M., Okura, R., Ide, W., Horimoto, S., Ezaki, K., Fujita, A., Shoda, K., Yokota, K.: Laser-detonation hyperthermal beam source applicable to VLEO environmental simulations. *CEAS Space J.* **2021**, 2 (2021)
17. Tagawa M., Okura R., Yokota K.: Reduced dissociation of molecules in laser-detonation-driven hyperthermal beams. In: *Proc. Adv.Space Environ. Conf., Universal City USA* (2019)
18. Yusuke, Y., Tani, Y., Tsukizaki, R., Koda, D., Nishiyama, K.: Characterization of plasma and gas in microwave discharge ion thruster  $\mu 10$  using kinetic particle simulation. *Trans. JSASS Aerosp. Tech. Jpn.* **18**, 57–63 (2020)
19. Ozawa T., Imamura S., Nishiyama K., Tagawa M., Fujita K.: Numerical analyses of air intake for air breathing ion engine, JAXA-SP-18-005, pp. 97–101 (2019)

**Publisher's Note** Springer Nature remains neutral with regard to jurisdictional claims in published maps and institutional affiliations.